

# Incommensurable matter-wave jets in quasi-1D geometry

Tadej Mežnaršič,<sup>1,2,\*</sup> Rok Žitko,<sup>1,2</sup> Katja Gosar,<sup>1,2</sup> Katja Arh,<sup>1,2</sup> Matevž Jug,<sup>1,2</sup> Erik Zupanič,<sup>1,3</sup> and Peter Jeglič<sup>1,2,†</sup>

<sup>1</sup>*Jožef Stefan Institute, Jamova 39, SI-1000 Ljubljana, Slovenia*

<sup>2</sup>*Faculty of mathematics and physics, University of Ljubljana, Jadranska 19, SI-1000 Ljubljana, Slovenia*

<sup>3</sup>*Faculty of natural sciences and engineering, University of Ljubljana, Aškerčeva 12, SI-1000 Ljubljana, Slovenia*  
(Dated: October 10, 2023)

We experimentally show the formation of incommensurable “golden”  $\frac{1+\sqrt{5}}{2}$  matter-wave jets in a Bose-Einstein condensate (BEC) subjected to single frequency interaction modulation. We study the formation of higher order jets and the corresponding incommensurable density waves in quasi one dimensional (1D) geometry with the help of numerical 1D Gross-Pitaevskii equation simulation. We explore the process of jet formation experimentally and theoretically for a large range of modulation amplitudes and frequencies and present a phase diagram for jet formation. In simulation, for large modulation amplitudes, the distribution of jet velocities forms a supercontinuum, which emerges from the observed incommensurable matter-wave jets.

Incommensurability is encountered in aperiodic crystals with incommensurable phases [1–3], charge and spin structures [4–8], twisted moiré bilayer experiments [9] with Hofstadter butterfly energy structure [10], and surface layers [11]. In the context of cold atoms, incommensurable optical lattices have been used to study wavefunction localization phenomena in disordered potentials within the Aubry-André model [12–20].

In this Letter we experimentally show the formation of incommensurable density waves inside a cesium BEC confined in a quasi one-dimensional (1D) potential evidenced via the emission of matter-wave jets. Previous studies of matter-wave jets in two dimensions have revealed the formation of density waves inside the condensate prior to the emission of jets and explained the process of formation of higher-order jets [21, 22]. We expand on our previous experiments with matter-wave jets in a quasi-1D potential [23] by experimentally and numerically exploring the formation of incommensurable “golden” jets and other higher-order jets in a quasi-1D BEC under a single-frequency interaction modulation.

We start by preparing an almost pure BEC of approximately 4000 cesium atoms in a crossed dipole trap, from which we release it into a channel with radial frequency  $\omega_r = 2\pi \cdot 90$  Hz. Simultaneously, we change the interaction between the atoms to  $a_{dc}$  close to zero via the wide  $s$ -wave Feshbach resonance [23], with zero-crossing at 17.1 G. This way we prepare a BEC soliton. For 4000 atoms the BEC forms a soliton at interaction  $a_{dc} = -2.7a_0$  [24]. To induce the emission of matter-wave jets, we modulate the magnetic field and therefore the interaction between the atoms as  $a(t) = a_{dc} + a_{ac} \sin(\omega t)$  for time  $t_p$ , where  $a_{ac}$  and  $\omega$  are the amplitude and the frequency of the modulation, respectively [25]. We let the system evolve for  $t_e$  in the channel and then we take an absorption picture after a 15 ms time-of-flight. The results are shown in Fig. 1(a). In addition to previously observed jets of first (J1) and second order (J2) [23], we observe two pairs of

jets with dimensionless velocities

$$u_{G2} = \frac{v_{G2}}{v_0} = \pm \frac{1 \pm \sqrt{5}}{2}, \quad (1)$$

where  $v_0 = \sqrt{\hbar\omega/m}$  is the velocity of the first-order jets (J1),  $\hbar$  is the reduced Planck constant, and  $m$  is the mass of an atom. We name these “golden jets” (G2) for their golden ratio dimensionless velocities. The irrational velocity ratio between first order and golden jets implies the existence of two incommensurable density waves inside the condensate prior to jet emission. Fig. 1(a) shows

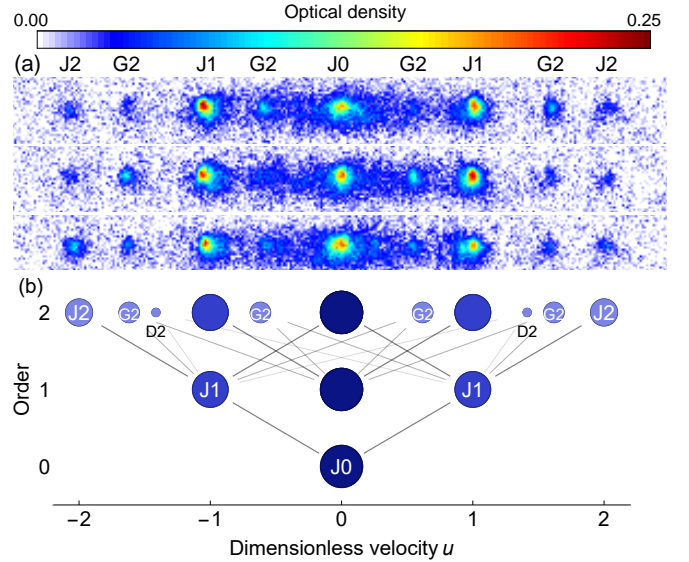


FIG. 1. (a) Absorption images of three different realizations of golden jets (for modulation frequency 4 kHz, amplitude  $a_{ac} = 90a_0$ ,  $t_p = 10$  ms, and  $t_e = 40$  ms). We see the original BEC (J0), first order jets (J1), second order jets (J2) and two pairs of “golden” jets (G2) (but not  $\sqrt{2}$  D2 jets). Each image shows an area of  $1037 \mu\text{m} \times 107 \mu\text{m}$ . (b) Schematic of possible jets for increasing number of subsequent collisions (order, encoded by color).

TABLE I. Jet orders, abbreviations, and formation processes. Beyond 2<sup>nd</sup> order, only jets observed in the simulations are included.

Order	Abbrev.	Formation process $(u_1, u_2) \rightarrow (u'_1, u'_2)$
0 <sup>th</sup>	J0	/
1 <sup>st</sup>	J1	$(0, 0) \rightarrow (-1, 1)$
2 <sup>nd</sup>	J2	$\pm(1, 1) \rightarrow (0, \pm 2)$
	G2	$(0, \pm 1) \rightarrow \pm \left( \frac{1-\sqrt{5}}{2}, \frac{1+\sqrt{5}}{2} \right)$
	D2	$(-1, 1) \rightarrow (-\sqrt{2}, \sqrt{2})$
3 <sup>rd</sup>	J3	$\pm(2, 2) \rightarrow \pm(1, 3)$
	G3	$\pm(1, 2) \rightarrow \pm \left( \frac{3-\sqrt{5}}{2}, \frac{3+\sqrt{5}}{2} \right)$

three experimental realizations of golden jets. As can be seen in Fig. 1(a) the golden jets are not necessarily symmetric around J0 and change in each experimental run despite the symmetry of involved processes. We attribute this to the asymmetry in the initial BEC which fluctuates between experimental runs

The origin of golden jets can be understood from the conservation of energy  $\frac{mv_1^2}{2} + \frac{mv_2^2}{2} + \hbar\omega = \frac{mv_1'^2}{2} + \frac{mv_2'^2}{2}$ , and momentum:  $mv_1 + mv_2 = mv_1' + mv_2'$ , where  $v_i$  ( $v_i'$ ) are the initial (final) velocities of the atoms. A pair of atoms in J1 is formed from a pair of colliding atoms from the original condensate (J0) by absorbing one quantum of energy from the modulating magnetic field. Similarly, a pair J0-J2 forms from a pair of J1 atoms with the same velocity and a pair G2-G2 from a pair J0-J1. In general the final velocities of the resulting jets are

$$u'_{1,2} = \frac{(u_1 + u_2) \pm \sqrt{(u_1 - u_2)^2 + 4}}{2}, \quad (2)$$

where  $u_{1,2}$  are the initial velocities of the atom pair. With each absorbed photon the number of possible jets increases. By the number of photons that an atom in a jet has absorbed we define the order of the jets: the initial BEC is zeroth order, J1 are first order, J2, G2 and others that form from them are second order and so on, see Fig. 1(b) and Table I. The total number of jets increases as a double exponential with order, going as 1, 3, 11, 109, 11605, ..., and can be approximately calculated as  $1.7949^{2^n}$  (from the fit up to  $n = 4$ , where  $n$  is the order). Experimentally, we observe J1, J2 and G2, but we haven't been able to observe jets with dimensionless velocity  $\pm\sqrt{2}$  (D2, the other second order jets) or any third order jets. J2 are formed from J1 which move with the same velocity so the process is equivalent to the primary process in a moving frame, while the atoms that form G2 move relative to each other, which reduces the interaction time, making golden jets rare. For D2 the ve-

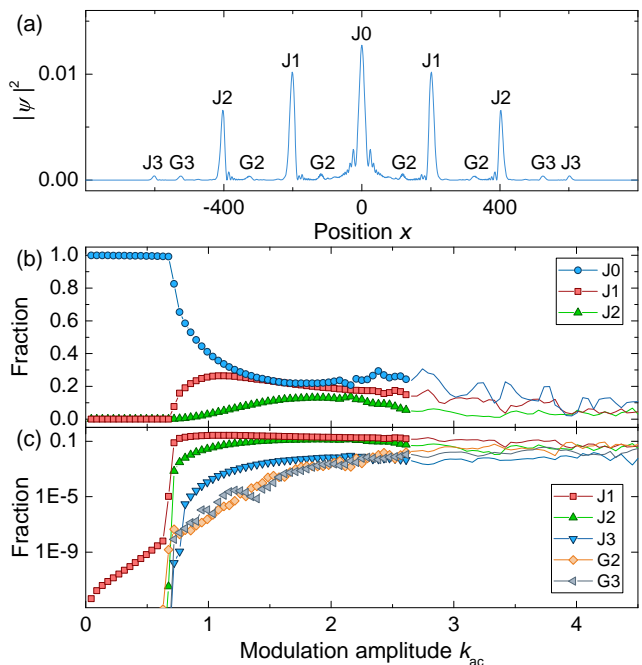


FIG. 2. (a) Final profile ( $t = 40$ ) of the simulation for  $\omega = 24$ ,  $k_{dc} = -0.045$ ,  $k_{ac} = 2.34$ ,  $t_p = 8\pi$  and the fraction of atoms in different jets (calculated as integrals on the interval  $(-20, 20)$  around the selected peaks in (b) linear and (c) logarithmic scale. Bare lines without symbols indicate the supercontinuum regime.

locity difference is two times higher, explaining why we don't observe them.

We turn to numerical simulations of 1D Gross-Pitaevskii equation (GPE) to better understand the conditions for the formation of each order of jets. Like in our previous work [23], we start with a soliton as the initial state and modulate the interaction parameter  $k(t) = Na(t)/a_r = k_{dc} + k_{ac} \sin(\omega t)$  for a time  $t_p = 8\pi$  with different frequencies  $\omega$  and amplitudes  $k_{ac}$ . We leave the wavefunction to evolve for  $t_e$  and look at the density profile  $n(x) = |\psi(x)|^2$ . In the simulations, time  $t$  is given in units  $1/\omega_r$ ,  $\omega$  in units  $\omega_r$ , and distances in units  $a_r = \sqrt{\hbar/m\omega_r}$ .

An example of the final density profile can be seen in Fig. 2(a) where all visible jets are marked. In contrast with the experiment, we observe additional jets of third order J3 and G3 which form from J2-J2 and J1-J2 pairs, respectively. Surprisingly, G2 and G3 have comparable amplitude even though G2 jets are second order whereas G3 only arise in third order; this seems to be due to the large amplitude of J2 jets (from which G3 are formed) in the simulation.

To quantify the size of jets, we calculate the integrals over a fixed interval around each peak in the density profile, which gives the fraction of the atoms in jets of each order (total integral is normalized,  $\int |\psi(x)|^2 dx = 1$ ). The

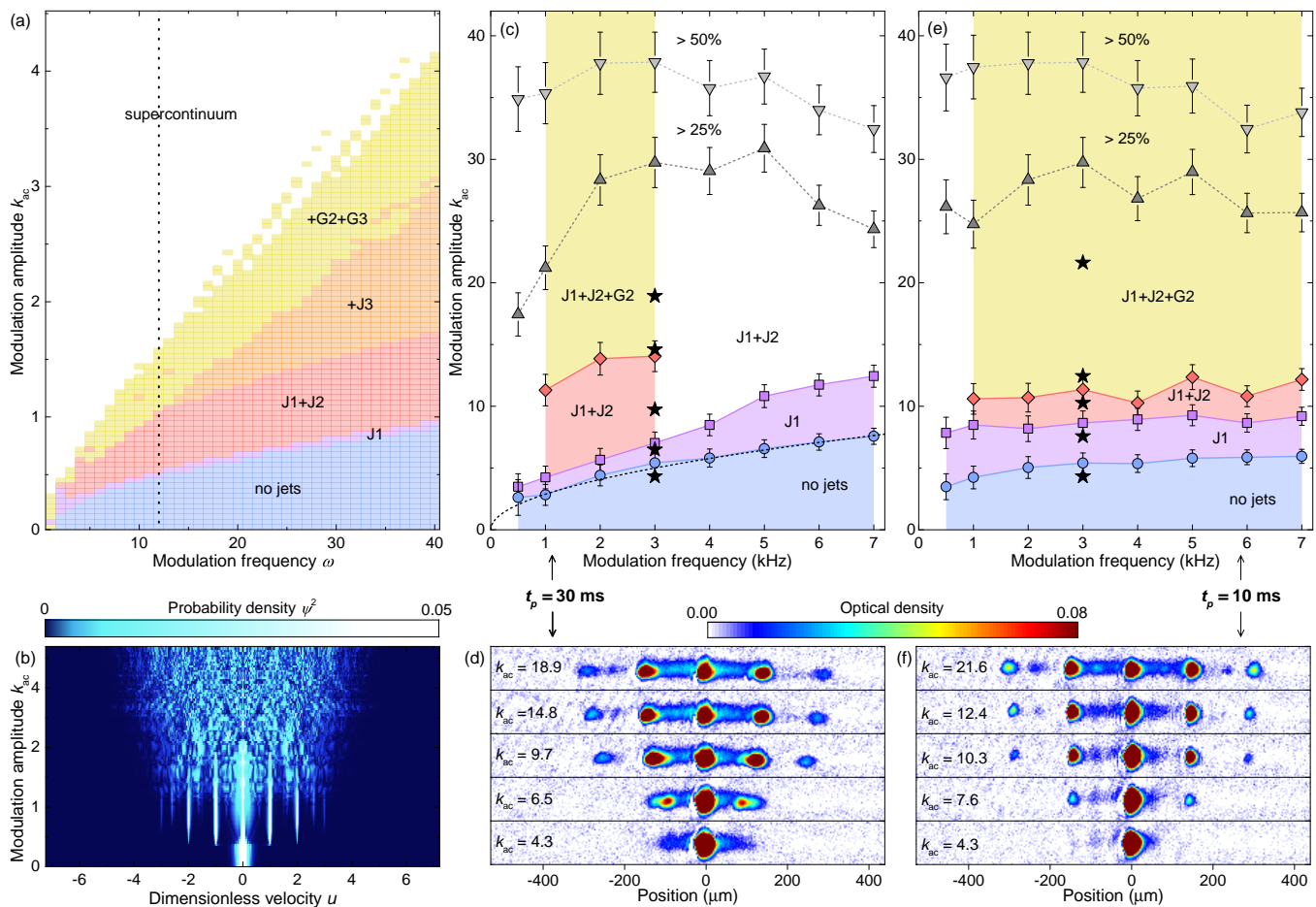


FIG. 3. (a) Phase diagram of jets from GPE simulations. The narrow band between “no jets” and “J1 + J2” is the region with only J1 jets. (b) Final density profiles in momentum space  $|\psi(q)|^2$  ( $t = 30$ ) for  $\omega = 12$  [along the dotted line in (a)]. (c) and (e) Experimental phase diagram of jets, measured at  $t_p = 30$  ms and 10 ms. The grey lines indicate where the number of atoms falls by 25% and 50% from the initial number of atoms in the condensate. The dashed black line in (c) is a fit to the boundary between the “no jets” and “J1” region, proportional to  $\omega^{1/2}$ . The errorbars correspond to the variance of the atom number and how precisely we can determine the amplitude corresponding to the boundary between regions. (d) and (f) Averages of 50 absorption images, as examples of different points in the phase diagram (marked with black stars in the diagrams above). From bottom to top the images represent regions with: no jets, only J1, J1 and J2, and J1, J2 and G2 (top two images). The images were taken for evolution time  $t_e = 42.7$  ms.  $k_{ac} = Na_{ac}/a_r$ , where  $N = 4000 \pm 200$  is the number of atoms in the BEC, before we start modulation.  $a_{ac}$  is calculated from the amplitude of the pulse by a calibration determined using the Feshbach resonance (details in Supplemental Material).

fraction in the central peak J0 only starts decreasing after the threshold amplitude for J1 formation is reached, as can be seen in Fig. 2(b). The J1 first increases steeply with amplitude and then levels out due to J0 depletion and losses to the higher-order processes. It can be seen that only the first order has a sharp threshold (Fig. 2(b)), while the higher orders increase smoothly from zero once the first order exists (Fig. 2(c)). D2 are not observed even in simulations due to the onset of a wide background at high amplitudes needed to create them (discussed below).

Based on calculated atom fractions, we construct a phase diagram of visibility of different set of jets, seen in Fig. 3(a). We declare that a new region begins when the fraction for the next jet exceeds 0.002. We choose this

value so that it is smaller than the fraction of the jets at high modulation amplitudes and much larger than the noise in the simulation. As the amplitude  $k_{ac}$  increases, additional jets are enabled and we transition into new regions. As discussed above the transitions are actually continuous and not discrete, except from the “no jets” to the “J1” region.

Fig. 3(b) shows the final profiles for a fixed frequency  $\omega = 12$ . The onset of J1, J2 and other jets can be clearly seen as the modulation amplitude increases. For very high amplitudes the discrete jets start disappearing in the increasingly uniform background of a multitude of higher order jets. The observed spread from the single momentum mode to a wide momentum distribution re-

sembles the generation of supercontinua in nonlinear optical media, where various instabilities cause an initially narrow frequency spectrum to disperse into a wide continuum [26]. The boundary for the supercontinuum can be determined from the median of the final density profile  $n(x)$ . It stays close to zero when we only have discrete jets and when it increases beyond 0.00025 we say that it has transitioned into the supercontinuum region (of course the transition is actually gradual, the threshold value was chosen to be above numerical noise and visually without separate jets). The threshold boundary for J1 formation is proportional to  $\omega^{1/2}$ , as previously reported [23, 25]. The fits to lower boundaries for J2 and J3 regions also give  $\omega^{1/2}$  dependences, while the boundaries for golden jets (G2+G3) and the supercontinuum region go as  $\sim \omega^{0.8}$ .

We explore the phase diagram of jet formation experimentally as well. Fig. 3(c) and (e) show the experimental phase diagrams of jet formation for modulation times  $t_p = 10$  ms and 30 ms, respectively. We determined the regions of the phase diagram where we observe J1, J1 and J2, and J1, J2 and G2.

In contrast to simulation, in the experiments, the number of atoms in jets varies from shot to shot; for example, see Fig. 1(a). This was previously observed in 2D [27], where the population in angular modes is also distributed. More information on the statistics of the number of atoms in each type of jet is available in the Supplemental Material (Fig. S3). Because of this variance, gathering statistics is necessary to determine the presence of the phase at each point in the phase diagram. We choose the boundary to be at the point where at least one image out of ten shows the corresponding jets. Examples of averages of 50 absorption images of jets from different parts of the phase diagram are shown below in Fig. 3(d) and (f) and in the Supplemental Material (Fig. S2). Note that the distance between the jets and the initial condensate varies for different modulation amplitudes. This is because jets are emitted sooner, if the modulation amplitude is higher.

The range of frequencies in the experimental and the theoretical phase diagram are similar (the frequencies shown in Fig. 3(a) range from 0 to 3.6 kHz, whereas the experimental phase diagrams in Fig. 3(c) and (e) were measured for frequencies between 1 kHz and 7 kHz). On the other hand, the values of  $k_{ac}$  required for excitation of jets are approximately ten times higher in the experiment than in simulation. This is most probably because the simulation describes a 1D system, and in the experiment, the BEC is a 3D object with jets confined into quasi-1D system by a dipole trap beam.

For  $t_p = 30$  ms, we are not even able to observe golden jets for modulation frequencies higher than 3 kHz even though, they are observable using the shorter  $t_p = 10$  ms. In the simulation, the modulation time is  $t_p = 8\pi$ , which corresponds to 44 ms. In the experiment, we

used shorter modulation times, because longer modulation times cause more atom losses and increase the incoherent background, formed by the excited atoms that are not part of the jets [23], making the occurrence of jets rarer and more difficult to observe (Supplemental Material Fig. S1 and S2). However, we see from the experimental phase diagrams that the shape of the threshold does depend on  $t_p$ . For a short  $t_p$  there is no strong dependence on the modulation frequency, whereas for the longer  $t_p$  the threshold boundary for the formation of jets is proportional to  $\omega^{1/2}$ , as expected from the simulation and previous experiments [23]. Additionally, the longer modulation times sometimes cause the jets to be emitted twice, making the interpretation of the absorption images less reliable.

As we increase the amplitude in the experiment, the total number of atoms starts decreasing and the incoherent background between the jets becomes stronger, as seen in Fig. 3, where we also plot the thresholds at which the total number of atoms is 25% and 50% smaller than the number of atoms in the initial BEC. The decrease in the number of atoms is likely due to partial collapses of the BEC, caused by the strong attractive interactions the BEC is subjected to during the modulation. The momentum distribution of the incoherent background also remains of the same width for increasing amplitude and does not increase beyond the position of J2 jets as the supercontinuum would. Atom losses and increased fraction of incoherent background, both absent from the simulation, decrease the effective modulation amplitude preventing the supercontinuum from forming.

In this work, we show the formation of matter-wave jets with golden ratio dimensionless velocity  $u_{G2} = (1 + \sqrt{5})/2$ , which form when a BEC in a quasi-1D geometry is subjected to a single-frequency interaction modulation. These jet velocities and the corresponding density waves are not commensurate with previously observed jets with dimensionless velocities  $u_{J1} = 1$  and  $u_{J2} = 2$ . It needs to be noted, that the occurrence of incommensurate density waves can easily be achieved with two-frequency driving, but here it emerges from single-frequency driving. Numerically and experimentally, we explore the formation of incommensurable jets for a wide range of modulation frequencies and amplitudes, resulting in a phase diagram of possible jets, while also uncovering an unexpected supercontinuum region. The supercontinuum likely arises due to the double-exponential growth of the number of possible modes, while the wavenumber only grows linearly, resulting in a densely populated momentum space. The supercontinuum is potentially experimentally observable if the three-body losses and the incoherent background could be reduced by increasing the radial trapping frequency, making the system more 1D. The demonstrated formation of incommensurable matter-wave jets could, for example, be used in multispecies experiments. The incommensu-

rable density waves inside one species could be used as a disordered potential for the other species, if the jets are prevented from escaping the trap (provided there exist appropriate Feshbach resonances). This would eliminate the need for an external disordered potential and even a regular lattice that is usually needed to capture impurities, which act as a source of disorder [12–20].

We thank Cheng Chin and Matjaž Gomilšek for helpful discussions. We would also like to thank Samo Beguš and Davorin Kotnik for their help with electronics. This work was supported by the Slovenian Research Agency (research core Grants No. P1-0125, No. P1-0099 and P1-0416, and research projects No. J2-8191 and No. J2-2514).

---

\* tadej.meznarsic@ijs.si

† peter.jeglič@ijs.si

- [1] P. Bak, Reports on Progress in Physics **45**, 587 (1982).
- [2] R. Lifshitz, Zeitschrift für Kristallographie **222**, 313 (2007).
- [3] T. Janssen, Acta Crystallographica Section A Foundations of Crystallography **68**, 667 (2012).
- [4] Y. Feng, J. Wang, D. M. Silevitch, B. Mihaila, J. W. Kim, J.-Q. Yan, R. K. Schulze, N. Woo, A. Palmer, Y. Ren, J. van Wezel, P. B. Littlewood, and T. F. Rosenbaum, Proceedings of the National Academy of Sciences **110**, 3287 (2013).
- [5] B. Keimer, S. A. Kivelson, M. R. Norman, S. Uchida, and J. Zaanen, Nature **518**, 179 (2015).
- [6] Y. Wang, B. Ge, Y. Cui, R. Yu, S. Chen, and Z. Ren, Materials Today Physics **5**, 7 (2018).
- [7] H. Miao, R. Fumagalli, M. Rossi, J. Lorenzana, G. Seibold, F. Yakhou-Harris, K. Kummer, N. B. Brookes, G. D. Gu, L. Braicovich, G. Ghiringhelli, and M. P. M. Dean, Physical Review X **9**, 031042 (2019).
- [8] G. Storeck, J. G. Horstmann, T. Diekmann, S. Vogelgesang, G. von Witte, S. V. Yalunin, K. Rossnagel, and C. Ropers, Structural Dynamics **7**, 034304 (2020).
- [9] S. Carr, S. Fang, and E. Kaxiras, Nature Reviews Materials **5**, 748 (2020).
- [10] X. Lu, B. Lian, G. Chaudhary, B. A. Piot, G. Romagnoli, K. Watanabe, T. Taniguchi, M. Poggio, A. H. MacDonald, B. A. Bernevig, and D. K. Efetov, Proceedings of the National Academy of Sciences **118**, 10.1073/pnas.2100061118 (2021).
- [11] Y. Hu, T. Zhang, D. Zhao, C. Chen, S. Ding, W. Yang, X. Wang, C. Li, H. Wang, D. Feng, and T. Zhang, Nature Communications **13**, 10.1038/s41467-022-28104-2 (2022).
- [12] J. E. Lye, L. Fallani, C. Fort, V. Guarrera, M. Modugno, D. S. Wiersma, and M. Inguscio, Physical Review A **75**, 061603(R) (2007).
- [13] G. Roati, C. D’Errico, L. Fallani, M. Fattori, C. Fort, M. Zaccanti, G. Modugno, M. Modugno, and M. Inguscio, Nature **453**, 895 (2008).
- [14] L. Fallani, C. Fort, and M. Inguscio, in *Advances In Atomic, Molecular, and Optical Physics* (Elsevier, 2008) pp. 119–160.
- [15] P. Bordia, H. Lüschen, S. Scherg, S. Gopalakrishnan, M. Knap, U. Schneider, and I. Bloch, Physical Review X **7**, 041047 (2017).
- [16] M. Schreiber, S. S. Hodgman, P. Bordia, H. P. Lüschen, M. H. Fischer, R. Vosk, E. Altman, U. Schneider, and I. Bloch, Science **349**, 842 (2015).
- [17] C. D’Errico, E. Lucioni, L. Tanzi, L. Gori, G. Roux, I. P. McCulloch, T. Giamarchi, M. Inguscio, and G. Modugno, Physical Review Letters **113**, 095301 (2014).
- [18] B. Gadway, D. Pertot, J. Reeves, M. Vogt, and D. Schneble, Physical Review Letters **107**, 145306 (2011).
- [19] J. Lin, J. Nan, Y. Luo, X.-C. Yao, and X. Li, Physical Review Letters **123**, 233603 (2019).
- [20] J. B. Reeves, B. Gadway, T. Bergeman, I. Danshita, and D. Schneble, New Journal of Physics **16**, 065011 (2014).
- [21] H. Fu, L. Feng, B. M. Anderson, L. W. Clark, J. Hu, J. W. Andrade, C. Chin, and K. Levin, Phys. Rev. Lett. **121**, 243001 (2018).
- [22] Z. Zhang, K.-X. Yao, L. Feng, J. Hu, and C. Chin, Nat. Phys. **16**, 652 (2020).
- [23] T. Mežnaršič, R. Žitko, T. Arh, K. Gosar, E. Zupanič, and P. Jeglič, Phys. Rev. A **101**, 031601(R) (2020).
- [24] T. Mežnaršič, T. Arh, J. Brence, J. Pišljarič, K. Gosar, Ž. Gosar, R. Žitko, E. Zupanič, and P. Jeglič, Phys. Rev. A **99**, 033625 (2019).
- [25] L. W. Clark, A. Gaj, L. Feng, and C. Chin, Nature **551**, 356 (2017).
- [26] J. M. Dudley, G. Genty, and S. Coen, Reviews of Modern Physics **78**, 1135 (2006).
- [27] J. Hu, L. Feng, Z. Zhang, and C. Chin, Nat. Phys. **15**, 785 (2019).